

The emergence of bubble-induced scaling in thermal spectra in turbulence

On-Yu Dung¹, Pim Waasdorp¹, Chao Sun^{1,3}, Detlef Lohse^{1,2}, and Sander G. Huisman^{1†}

¹Physics of Fluids Group, J. M. Burgers Center for Fluid Dynamics, and Max Planck Center Twente, Faculty of Science and Technology, University of Twente, P.O. Box 217, 7500 AE Enschede, The Netherlands

²Max Planck Institute for Dynamics and Self-Organization, Am Fassberg 17, 37077 Göttingen, Germany

³Center for Combustion Energy, Key Laboratory for Thermal Science and Power Engineering of Ministry of Education, Department of Energy and Power Engineering, Tsinghua University, 100084 Beijing, China

(Received xx; revised xx; accepted xx)

We report on the modification of the spectrum of a passive scalar inside a turbulent flow by the injection of large bubbles. While the spectral modification through bubbles is well known and well analyzed for the velocity fluctuations, little is known on how bubbles change the fluctuations of a passive scalar. Here we uncover the thermal spectral scaling behavior of a turbulent multiphase thermal mixing layer. We trigger the development of a -3 spectral scaling by injecting large bubbles ($Re_{bub} = \mathcal{O}(10^2)$) with gas volume fractions up to 5%. For these bubbly flows, the $-5/3$ scaling is still observed at intermediate frequencies but it is followed by a steeper slope for larger frequencies. This -3 scaling range extends with increasing gas volume fraction. The -3 scaling experiment coincides with the typical energy spectral scaling for the velocity fluctuations in high Reynolds number bubbly flow. We identify the frequency scale of the transition from the $-5/3$ scaling to the -3 scaling and show how it depends on the gas volume fraction.

Key words: multiphase flow, turbulence, bubbles, heat transfer, passive scalar, temperature

1. Introduction

In fully developed turbulent flows, universality is observed for velocity and temperature fluctuations. According to the Kolmogorov–Obukhov–Corrsin theory (Kolmogorov (1941); Obukhov (1949); Corrsin (1951)) and verified extensively in experiment and numerical simulations, the universal scaling of the spectrum of a scalar exhibits a $-5/3$ scaling ($E_\theta(k) \propto k^{-5/3}$) in the inertial-convective range for high enough Reynolds and Péclet number (see e.g. Monin & Yaglom (1975)). Here k is the wavenumber and θ is a passive scalar (Monin & Yaglom (1975)) such as the concentration of a chemical substance or the temperature, in case that buoyancy is not relevant. If additional complexity is added to the system, different scaling phenomena can appear, such as having an active scalar introducing buoyancy effects (e.g. Rayleigh–Bénard convection) (Lohse & Xia

† Email address for correspondence: s.g.huisman@utwente.nl

(2010)), adding visco-elasticity to the carrier liquid (Steinberg (2020)), or by adding finite particles (Risso (2018) and Brandt & Coletti (2022)) or bubbles (Balachandar & Eaton (2010); Risso (2018); Lohse (2018); Mathai *et al.* (2020)). In this work, we do the latter and introduce a large number of finite-size rising bubbles to the liquid flow (Balachandar & Eaton (2010); Risso (2018); Lohse (2018); Mathai *et al.* (2020)). Large rising bubbles are defined here as having a bubble Reynolds number $Re_{bub} = V_r d / \nu = \mathcal{O}(10^2)$, where V_r is the bubble rise velocity relative to the mean vertical velocity of the carrier liquid, d is the mean area-equivalent bubble diameter (as compared to a spherical bubble), and ν is the kinematic viscosity of the carrier liquid.

First observed and theoretically addressed in Lance & Bataille (1991), the introduction of bubbles lead to the emergence of a k^{-3} scaling of the velocity fluctuation (energy) spectra $E_u(k)$. They argued that in a statistical steady state, the k^{-3} scaling in the spectrum can be achieved by balancing the viscous dissipation and the energy production due to the rising bubbles in the spectral space (Lance & Bataille (1991)). The k^{-3} scaling can also result from spatial and temporal velocity fluctuations in homogeneous bubbly flows (Risso (2018)), and is found to be robust and is observed for a homogeneous bubble swarm for a wide range of parameters: $10 \leq Re_{bub} \leq 1000$ and $1 \leq We \leq 4$ where We is the Weber number (Risso (2018); Pandey *et al.* (2020)). In contrast, point particle simulations do not show k^{-3} scaling (Mazzitelli & Lohse (2009)), because the wakes behind the bubbles which are obviously absent for point particles are crucial for the emergence of a -3 scaling (in either frequency or wavenumber space).

While there are abundant studies on the energy spectra in high-Re bubbly flow, the study of scalar spectra in such flow is limited. Alméras *et al.* (2016) investigated the time-resolved concentration fluctuations of a fluorescent dye (passive scalar) in a confined bubbly thin cell in which the scalar spectral scaling f^{-3} is observed, where f is the frequency. For the three-dimensional case, Gvozdić *et al.* (2018) investigated the scalar spectra in a bubbly column in a vertical convection setup, but they were unable to resolve the frequencies related to the -3 scaling of the energy spectra in bubble-induced turbulence (Gvozdić *et al.* (2018)).

In the present experimental work, by utilizing a fast-response temperature probe, we are able to capture the gradual change of the *passive scalar* spectral scaling for increasing bubble concentration α in a bubbly turbulent thermal mixing layer. In addition, we will investigate the transition scale of the -3 scaling as it illuminates the physical origin of the -3 subrange of both the scalar and the energy spectra. The transition frequency to the -3 subrange for energy spectra indeed has yet to be exactly identified (Risso (2018)).

2. Experimental setup and methods

We utilize the Twente Mass and Heat Transfer Tunnel (Gvozdić *et al.* (2019)) which creates a turbulent vertical channel flow, and allows for injecting bubbles and heating the liquid in a controlled manner. The turbulence is actively stirred using an active grid, see Fig. 1a. Using this facility we create a turbulent thermal mixing layer (de Bruyn Kops & Riley (2000)) in water with a mean flow velocity of approximately 0.5 m/s, resulting in a Reynolds number of $Re = 2 \times 10^4$. The global gas volume fraction α in the measurement section is measured by a differential pressure transducer of which the two ends are connected to the top and bottom of the measurement section. A fast-response thermistor (Amphenol Advanced Sensors type FP07, with a response time of 7 ms in water) is placed into the middle of the measurement section in order to measure the temperature. An AC bridge with a sinusoidal frequency of 1.3 kHz drives the thermistor in order to reduce electric noise. The bridge potential is measured by a lock-in amplifier (Zurich Instruments

MFLI). A temperature-controlled refrigerated circulator with water bath (PolyScience PD15R-30) with a temperature stability of ± 0.005 K is used for calibrating the thermistor. By fitting the temperature-resistance characteristic equation proposed by Steinhart & Hart (1968) over a short range of temperature of interest (in which the terms are kept only up to the first order to avoid over-fitting), the thermistor has a relative precision of 1 mK. This temperature uncertainty is propagated from the uncertainties of the fitting parameters of the Steinhart-Hart equation. The typical large-scale temperature difference from the heated side to the non-heated side at the mid-height of the measurement section of height $h = 1$ m is about 0.2 K. The working liquid is decalcified tap water at around 22.7 °C, with a Prandtl number $\text{Pr} = \nu/\kappa = 6.5$, where ν and κ are the kinematic viscosity and thermal diffusivity of water, respectively.

For the velocity measurements, we employ constant temperature anemometry (CTA) using a hot film sensor (Dantec 55R11, 70 μm diameter with a 2 μm nickel coating, 1.3 mm long and up to 30 kHz frequency response) placed in the middle of the tunnel. We note that since a CTA measurement requires negligible temperature variation of the flow, the velocity is measured when the heaters are switched off. The velocity statistics are not influenced by the temperature because the fluctuations in the flow are completely dominated by the turbulence generated by the active grid and upward mean flow rather than by buoyancy caused by density differences due to the temperature differences. To substantiate this statement, we must compare the relative importance of the buoyancy force (parallel to the streamwise direction) to the inertial force due to the advection of a passive scalar. The ratio of these forces equals the ratio of the Grashof number Gr and the square of the Reynolds number $\text{Re}_{0.5h}^2$ (Schlichting & Gersten (2017)). Here we base these numbers on the vertical distance between $\pm 0.25h$ from the middle of the measurement section, the temperature difference across such height $\Delta_{0.5h} \leq 50$ mK and the mean liquid velocity $U = 0.5 \text{ ms}^{-1}$. This gives $\text{Gr}/\text{Re}_{0.5h}^2 = 0.5hg\beta\Delta_{0.5h}/U^2 \leq \mathcal{O}(10^{-3})$, where g and β are the gravitational constant and volumetric expansion coefficient of water, respectively. The small value of this ratio implies that the temperature can be seen as passive scalar under our flow conditions.

Next, we present the turbulent characteristics in the single-phase turbulent thermal mixing layer. Laser Doppler anenomemtry (LDA) (Dantec) is used for measuring the horizontal (u_x) and vertical (u_z) velocity in order to characterise the velocity fluctuations. We denote the velocity fluctuations of the liquid in single-phase as u'_0 and approximate $u'_0 \approx u'_z$, where the prime velocities refer to the standard deviations of the standard deviation of the velocity components. The viscous dissipation rate ϵ is estimated by finding the longitudinal second order structure function (measured by CTA and used Taylor's frozen flow hypothesis) and using the velocity two-third law which is valid in the inertial range (Pope (2000)). We then obtain the Kolmogorov length scale $\eta = (\nu^3/\epsilon)^{1/4} = 0.22 \text{ mm}$ and the dissipation time scale $\tau_\eta = (\nu/\epsilon)^{1/2} = 49 \text{ ms}$. To estimate the scalar dissipation rate ϵ_θ , similarly we use the temperature (scalar) two-third law (Monin & Yaglom (1975)). Let also λ_u and λ_θ be the Taylor-microscale of the velocity and the temperature, respectively (Yasuda *et al.* (2020)). Isotropy is assumed to estimate the order of magnitude of λ_u and λ_θ . We find that our turbulent thermal mixing layer, for the single phase case, has a Taylor Reynolds number of $\text{Re}_{\lambda_u} = u'_0\lambda_u/\nu = 130$ and the Péclet numbers based on both microscales are $\text{Pe}_{\lambda_u} = u'_0\lambda_u/\kappa = 870$ and $\text{Pe}_{\lambda_\theta} = u'_0\lambda_\theta/\kappa = 520$ (Yasuda *et al.* (2020)). The traditional choice of the microscale is λ_u (Mydlarski & Warhaft (1998)) but numerical simulations have uncovered that the small-scale anisotropy of the scalar field depends on the Péclet number based on λ_θ (Yasuda *et al.* (2020)). So here we give both values. We employ $\epsilon = C_\epsilon u'_0^3/L_u$, where $C_\epsilon = 0.9$ and L_u is the velocity integral length scale (Valente & Vassilicos (2012); Vassilicos (2015)), to

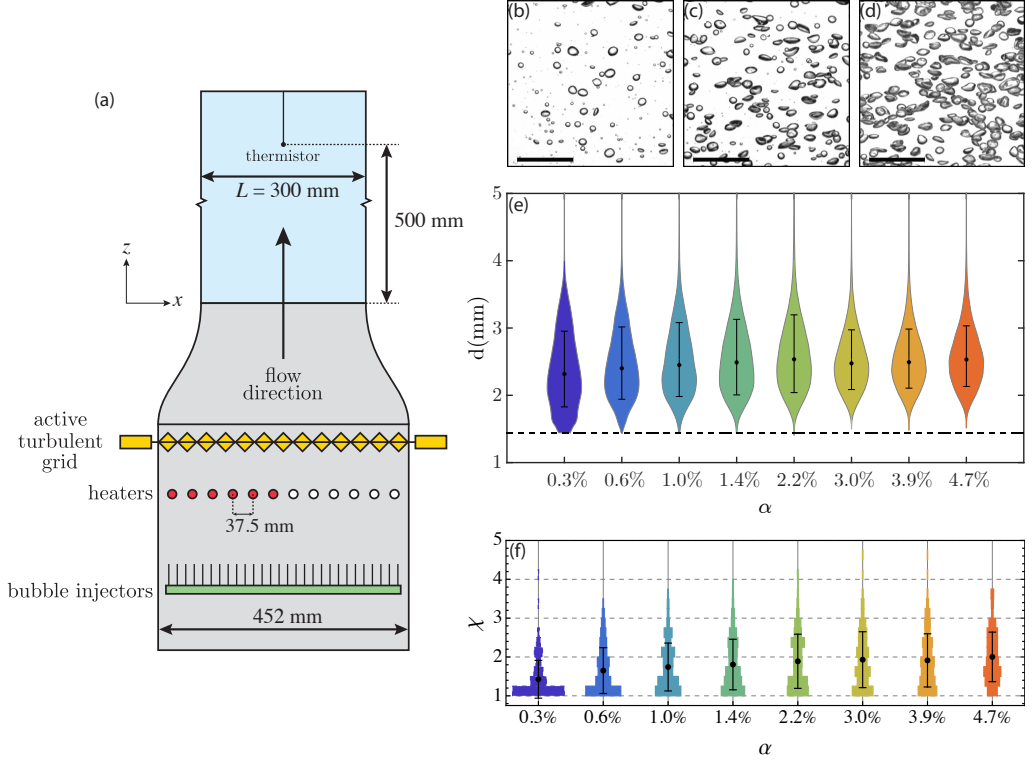


FIGURE 1. (a) Schematic of the experimental setup used in the current study. Bubbles are injected by 120 needles (green). The setup is equipped with 12 heaters. A power of 2250 W is supplied to the left half of the heaters (red), while the right half (white) is left unpowered, creating a turbulent thermal mixing layer. Each heating cartridge (Watlow, Firerod J5F-15004) has a diameter of 12.7 mm. The center-to-center distance between two consecutive heaters is 37.5 mm. The turbulence is stirred by an active grid with a total of 15 engines connected to diamond flaps (yellow) Gvozdić *et al.* (2019). The measurement section (blue area) has a height of 1.00 m, a width of 0.3 m, and is 0.04 m thick. (b,c,d) High speed snapshots of the bubble flow, as seen from the side for the volume fractions $\alpha = 0.3\%$, 1.4% , and 4.7% . Scale bars of 20 mm are added to each figure. (e) Distribution charts of the bubble diameter obtained using image analysis of high-speed footage for a variety of gas volume fractions α . The resolution of the footage prohibits us to measure the size of bubbles (dashed line) < 1.4 mm. Dots indicate the mean bubble diameter d . (f) Histograms of the bubble aspect ratio χ obtained by fitting the bubbles on the high-speed footage with ellipses. χ is defined as the ratio of the semi-major axis divided by the semi-minor axis. Each black dot represents the mean aspect ratio χ and each error bar represent one standard deviation of the distribution. See also Table 2 for the details of the bubble properties.

estimate L_u . As the mean temperature profile for the single-phase turbulent mixing layer follows a self-similar error-function profile (Ma & Warhaft (1986); de Bruyn Kops & Riley (2000)), we fitted the profile accordingly and obtain the large-scale characteristic length L_θ of the single-phase thermal mixing layer from the fitting parameters. The turbulent characteristics of the single-phase turbulent mixing layer are summarised in Table 1.

Bubbles are created by injecting regular air through needles, see Fig. 1a. Using high-speed imaging in a backlight configuration we characterize the size of our bubbles for a variety of volume fractions, see the example photos Figs. 1(b,c,d). We analyze the data by making use of the circular Hough transform to detect the individual (potentially overlapping) bubbles. We track the bubbles over time such as to obtain the mean bubble

| η (mm) | τ_η (ms) | η_θ (mm) | λ_u (mm) | λ_θ (mm) | Re_{λ_u} | Pe_{λ_u} | Pe_{λ_θ} | L_u (m) | L_θ (m) |
|-------------|------------------|--------------------|------------------|-----------------------|------------------|------------------|-----------------------|-----------|----------------|
| 0.22 | 49 | 0.085 | 4.9 | 2.1 | 130 | 870 | 520 | 0.04 | 0.15 |

TABLE 1. Relevant turbulent flow parameters of the single-phase turbulent thermal mixing layer in the current study ($\alpha = 0\%$, mean liquid flow speed = 0.5 m/s). For the definitions of the parameters, see Sec. 2.

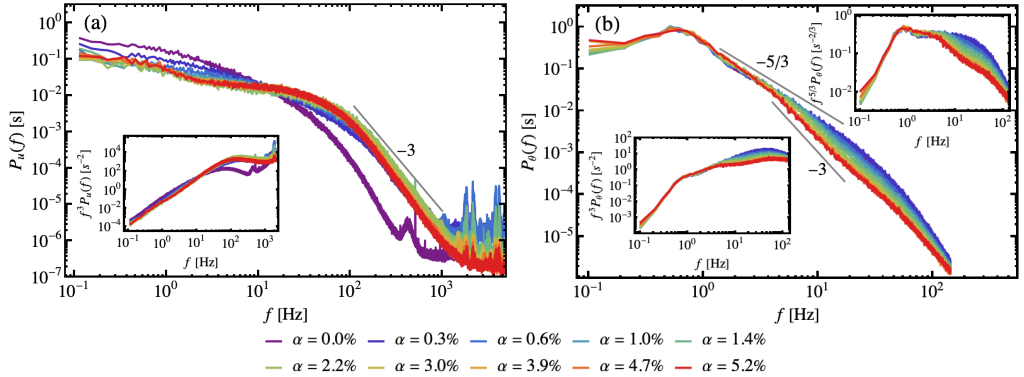


FIGURE 2. (color) $P_i(f)$, the power spectra normalised by their respective variance of (a) the velocity fluctuations ($P_u(f)$) and of (b) the temperature fluctuations ($P_\theta(f)$) for α from 0 % (purple) to 5.2% (red). The compensated spectra $f^3 P_i(f)$ and $f^{5/3} P_\theta(f)$ are shown as insets. The scalar spectra are cut at the limit of 143 Hz, corresponding to the highest resolved frequency of the thermistor.

rise velocity, see Table 2. In Fig. 1(e) we show the PDF of the bubble diameter for several α in the form of distribution charts. We observe that for $\alpha > 0.3\%$ the bubble distribution is hardly unchanged with a mean bubble diameter of $d \approx 2.5$ mm. The aspect ratio of the bubbles χ were obtained by fitting the bubbles with ellipses in the high-speed footage by hand using the software ImageJ. For each α , the number of bubbles used for fitting to obtain the aspect ratios is between 188 to 245. Fig. 1f shows χ versus α . The trend shows the mean to be almost monotonically increasing with α , saturated at high α . We will use these bubbles to provide additional stirring to the liquid.

For the cases with bubbles, since it is highly anisotropic between vertical and azimuthal directions, we estimate the velocity fluctuations of the liquid as $U' \equiv \sqrt{2\langle u_x'^2 \rangle + \langle u_z'^2 \rangle}$, where we assume $\langle u_x'^2 \rangle = \langle u_y'^2 \rangle$. We first explore the parameter space by increasing α from 0.0% to 5.2% for a fixed flow velocity of 0.5 m/s and with our active grid turned on. Finally, the bubble Reynolds number $Re_{\text{bub}} = V_r d / \nu$ as obtained from visualization is in the range between 480 ($\alpha = 0.6\%$) and 220 ($\alpha = 4.7\%$). The above properties of the bubbles are summarised in Table 2.

3. The energy and scalar spectra

As the scalar in the present study is advected passively by the liquid velocity, the corresponding energy spectra first need to be examined in order to understand the passive scalar spectra. In Fig. 2 we show the energy and scalar power spectra P_u and P_θ for different gas concentrations α , normalized by their corresponding variance, corresponding to the normalized energy and scalar power spectra, respectively. The method of calculating the spectra of the velocity and temperature fluctuations for two-

phase flows is discussed in Appendix A. The energy spectra for single-phase shows a limited inertial range. However, whenever $\alpha > 0$, a pronounced -3 scaling is observed with the presence of an energy ‘bump’ just before this -3 scaling when α is large enough, which is consistent with the results of Alm  ras *et al.* (2017). We find that such -3 scaling occurs roughly between 100 Hz to 1000 Hz and has a higher energy content than the single-phase in the same frequency range. The physical mechanism of such small-scale enhanced velocity fluctuations is attributed to bubble-induced agitations, in which the velocity fluctuations produced by the bubbles are directly dissipated by viscosity (Lance & Bataille (1991); Prakash *et al.* (2016); Risso (2018)).

Next, we examine the passive scalar (thermal) spectra. A scaling of $-5/3$ for $1 \text{ Hz} \leq f \leq 15 \text{ Hz}$ is observed for the single-phase scalar spectrum. The phenomenon that a developed inertial range is observed in a passive scalar spectrum but not in the corresponding energy spectrum due to limited Reynolds number was found previously by Jayesh *et al.* (1994). As opposed to the relative high frequency (small-scale) fluctuation enhancement in the energy spectra, the scalar spectra show relative high frequency (small-scale) diminution when α increases from zero. The $-5/3$ scaling is followed by a steeper slope when α increases but such change of scaling is gradual and approximately saturated to the scaling of -3 for high enough α ($\alpha \approx 4.7\%$) around $f = \mathcal{O}(10\text{Hz})$. The main differences between the energy and the passive scalar spectra are that the rising bubbles produce additional fluctuations in the former but diminish the fluctuations in the latter. As we will explain below, this can be understood due to the added small-scale mixing of the thermal fluctuations by the bubbles which smoothens the temperature field. The emergence of the -3 scaling is abrupt in the former but gradual in the latter; and the -3 scaling occurs at $\mathcal{O}(100\text{Hz})$ for the former but $\mathcal{O}(10\text{Hz})$ for the latter. Clearly, there are differences in the physical mechanisms that lead to the same -3 scaling for the energy and passive scalar spectra. We first clarify the physical and mathematical background before speculating on the emergence of the -3 scaling in the scalar spectra.

The main commonalities and differences of the physical settings of the velocity and temperature fields are as follows. One common aspect is that along the measurement section, both the viscosity and diffusivity reduce the velocity and temperature fluctuations, respectively. On the other hand, the mean velocity field is homogeneous in the bulk of the measurement section while the temperature field has a large-scale mean temperature gradient. The high-Re bubbles have viscous boundary layers at their air-water interface but there is negligible temperature difference between the bubbles and the liquid phase, thus no thermal boundary layers are formed at the air-water interface. The viscous boundary layers transport momentum to the liquid phase at the scale related to bubbles, producing velocity agitations. The absence of thermal boundary layers implies no heat transport is present at the scale related to bubbles. Therefore, the only source of scalar fluctuations is from the mean temperature gradient while the source of velocity fluctuations is from bubble agitations.

Mathematically, for the spectral behavior of a passive scalar, one can consider the general spectral equation for the three dimensional scalar spectra $E_\theta(k, t)$ derived from the advection-diffusion equation (Monin & Yaglom (1975)) which neglects viscous heating,

$$\frac{\partial}{\partial t} E_\theta(k, t) + 2\kappa k^2 E_\theta(k, t) = T_\theta(k, t) + \Pi_\theta(k, t), \quad (3.1)$$

where t is the time and T_θ and Π_θ are the local net transfer and the production at wave-number k respectively. One can employ Taylor’s frozen-flow hypothesis to transform from the frequency domain to the wavenumber domain. In the present case, for increasing α ,

the single-phase $-5/3$ scaling of the spectrum gradually transitions to a -3 scaling at higher k (or f).

With the above discussed physical settings and scaling behaviors, we now speculate on the physical mechanisms on the -3 scaling of the scalar spectra in bubbly flows. The $-5/3$ range is considered to be the inertial range where there is negligible net local transfer, negligible production and neglected diffusivity (and viscosity) effect (Lance & Bataille (1991)). The scalar production due to the mean temperature gradient occurs at a smaller frequency than the $-5/3$ frequency range (lower than 1 Hz). Since the production due to the presence of bubbles is negligible as discussed previously, we speculate that $\Pi_\theta \approx 0$ at the scalar -3 subrange. Furthermore, we speculate that the rising bubbles enhance the mixing of temperature by homogenizing the temperature with increasing α at the scale related to the bubbles, and thus we observe a faster drop (steeper slope) in the passive scalar spectra. When α is large enough, the smoothing of the temperature inhomogeneity due to the bubbles is so strong that the thermal fluctuations are *directly smoothed out* by the molecular thermal diffusivity which causes the saturation of the scaling. When this situation happens, and following Eq. 3.1, we speculate that $T_\theta = T_\theta(\epsilon_\theta, k)$, where ϵ_θ is the scalar fluctuation dissipation rate. From dimensional analysis, we find that $T_\theta \propto \epsilon_\theta k^{-1}$. For a statistical stationary state, we can rearrange the terms to obtain a $E_\theta \propto k^{-3}$ scaling. This derivation is similar to Lance & Bataille (1991) though they neglected the net local transfer term and performed dimensional analysis on the velocity fluctuation production by the bubbles instead.

4. Transition frequencies from $-5/3$ to -3 scaling

The frequencies corresponding to the onset of the -3 scaling of the scalar spectra are now examined. For large enough α , each spectrum exhibits a $-5/3$ scaling before a -3 scaling, see Fig. 3a for examples. We identify the onset frequency f_t by using the parameterization

$$P_\theta(f) = \frac{(f/f_L)^{\zeta_b}}{[1 + (f/f_t)^2]^{\frac{\zeta_b - \zeta_a}{2}}} \quad (4.1)$$

which captures a transition from one scaling to another. Here f_L is a fitting parameter which reflects the height of the curve, and f_t is the transition frequency from the scaling f^{ζ_b} (for $f \ll f_t$) to f^{ζ_a} (for $f \gg f_t$) with scaling exponents ζ_b and ζ_a , respectively, see Fig. 3. Here we do not fit these exponents, but set $\zeta_b = -5/3$ (Kolmogorov-Obukhov value) (Monin & Yaglom (1975)) and $\zeta_a = -3$, consistent with the exponent of the velocity spectra in high-Re bubbly flows (Risso (2018)) and reflecting the observed limiting cases. To determine the range that covers most of the $-5/3$ and -3 scaling, we examine the local logarithmic slope $\xi(f)$ of the scalar power spectra, which is given by

$$\xi(f) = \frac{d \log_{10} P_\theta(f)}{d \log_{10} f}. \quad (4.2)$$

| α (%) | U' (m/s) | d (mm) | We U' | χ | V_{bub} (m/s) | $\langle V_r \rangle$ (m/s) | $\langle \text{We}V_r \rangle$ | $\langle \text{Re}_{\text{bub}} \rangle$ | f_t (Hz) | f_L (Hz) | $f_{c,A}$ (Hz) |
|---------------|-------------------|---------------|-----------------|---------------|-----------------|-----------------------------|--------------------------------|--|----------------|-----------------|----------------|
| 0.3 ± 0.2 | — | 2.4 ± 0.5 | — | 1.4 ± 0.5 | 0.68 ± 0.14 | — | — | — | — | — | — |
| 0.6 ± 0.2 | 0.042 ± 0.008 | 2.5 ± 0.5 | 0.06 ± 0.03 | 1.6 ± 0.6 | 0.70 ± 0.13 | 0.194 ± 0.03 | 1.30 ± 0.04 | 512 ± 9 | — | — | 11.0 ± 0.4 |
| 1.0 ± 0.2 | 0.051 ± 0.007 | 2.5 ± 0.5 | 0.09 ± 0.03 | 1.7 ± 0.6 | 0.68 ± 0.11 | 0.179 ± 0.004 | 1.13 ± 0.04 | 480 ± 10 | 10.6 ± 0.7 | 0.54 ± 0.01 | 9.9 ± 0.4 |
| 1.4 ± 0.2 | 0.047 ± 0.006 | 2.6 ± 0.6 | 0.08 ± 0.03 | 1.8 ± 0.7 | 0.67 ± 0.11 | 0.164 ± 0.003 | 0.96 ± 0.03 | 448 ± 7 | 8.1 ± 0.5 | 0.55 ± 0.01 | 9.0 ± 0.3 |
| 2.2 ± 0.2 | 0.064 ± 0.005 | 2.6 ± 0.6 | 0.15 ± 0.04 | 1.9 ± 0.7 | 0.64 ± 0.11 | 0.148 ± 0.003 | 0.79 ± 0.04 | 411 ± 9 | 5.8 ± 0.3 | 0.58 ± 0.02 | 7.9 ± 0.4 |
| 3.0 ± 0.2 | 0.073 ± 0.006 | 2.5 ± 0.4 | 0.19 ± 0.04 | 1.9 ± 0.7 | 0.62 ± 0.11 | 0.130 ± 0.004 | 0.59 ± 0.04 | 350 ± 10 | 4.8 ± 0.3 | 0.57 ± 0.02 | 7.2 ± 0.4 |
| 3.9 ± 0.2 | 0.090 ± 0.006 | 2.5 ± 0.4 | 0.29 ± 0.06 | 1.9 ± 0.7 | 0.60 ± 0.11 | 0.117 ± 0.005 | 0.48 ± 0.04 | 320 ± 10 | 4.1 ± 0.2 | 0.60 ± 0.02 | 6.4 ± 0.5 |
| 4.7 ± 0.2 | — | 2.6 ± 0.5 | — | 2.0 ± 0.6 | 0.59 ± 0.11 | 0.090 ± 0.004 | 0.29 ± 0.028 | 250 ± 10 | 3.9 ± 0.2 | 0.59 ± 0.02 | 4.9 ± 0.5 |
| 5.2 ± 0.2 | — | — | — | — | — | — | — | — | 3.5 ± 0.2 | 0.61 ± 0.02 | — |

TABLE 2. Experimental parameters as a function of α : velocity fluctuations of the liquid $U' \equiv \sqrt{2u_x'^2 + u_z'^2}$ with primed velocities referring to the standard deviation of these velocity components, area-equivalent bubble diameter d , the Weber number based on the turbulent velocity U' for the bubbles $\text{We}_{U'} = \rho U'^2 d / \gamma$ (with γ the surface tension), the aspect ratio of the bubble diameter χ , the bubble rise velocity V_{bub} , the bubble relative (to the liquid phase) rise velocity $V_r \equiv V_{\text{bub}} - \langle u_z \rangle$, the mean Weber number based on the bubble relative rise velocity $\text{We}_{V_r} = \rho V_r^2 d / \gamma$, the bubble Reynolds number $\text{Re}_{\text{bub}} = V_r d / \nu$, the fitting parameters f_t and f_L (below Eq. 4.1), and $f_{c,A}$ (Eq. 4.3) Alméras *et al.* (2017). The bubble sizes and velocity are obtained by image analysis (see Sec. 2). The aspect ratio of the bubbles are obtained by fitting the bubbles with ellipses. The uncertainty of α stems from the precision of the differential pressure gauge (Gvoždić *et al.* (2019)). For U' , d , $\text{We}_{U'}$, χ , V_{bub} , we show the mean values and the corresponding standard deviations for the distributions. For V_r , We_{V_r} and Re_{bub} , we show the corresponding mean values and the standard errors of the mean. For f_L and f_t , we show the mean values and the corresponding confidence intervals for a 95% confidence level obtained from the fitting. For $f_{c,A}$, we show the mean values and the corresponding confidence intervals for a 95% confidence level.

To estimate the local logarithmic slope at different frequency, for each spectrum, a moving fit of a straight line in logarithmic space (centred at a frequency with a window size of one-fourth decade of the frequency) is employed in order to obtain a local logarithmic slope at that frequency. The results of $\xi(f)$ for different α are shown in Fig. 3b. In the figure, we see that at around 1.2 Hz, $-5/3$ scaling starts to develop and the -3 scaling ends at around 15 Hz for the highest gas volume fraction case ($\alpha = 5.2\%$). Therefore, 1.2 Hz to 15 Hz is a reasonable range that covers the transition from $-5/3$ to -3 scaling for all cases.

We fit the spectra of Fig. 2b with Eq. 4.1 with $\zeta_b = -5/3$ and $\zeta_a = -3$ only for the $\alpha \geq 1.0\%$ cases, since for $\alpha < 1\%$ the transition frequencies resulting from the fits are either outside the fitting range or very close to the boundary of the fitting range. The fits for $\alpha = 1.0\%$ and $\alpha = 5.2\%$ are shown in Fig. 3a. It shows qualitatively nice fits for $\alpha = 1.0\%$, even though this case does not exhibit a fully developed -3 scaling. The figure also shows that for the case of $\alpha = 5.2\%$ the scaling is close to -3 after the transition and that the transition frequency f_t is smaller for this higher value of α .

$$f_{c,A} = 0.14 \langle V_r \rangle / \langle d \rangle, \quad (4.3)$$

where we stress again that d is the *area-equivalent* diameter whereas in Riboux *et al.* (2013) the mean *volume-equivalent* diameter is used instead. Table 2 includes these values of $f_{c,A}$, which we are also shown Fig. 4.1c. Since the -3 scaling has not developed for low α and thus the identification of f_t for low α is hard to determine, we can only conclude that both f_c and f_t identified here have decreasing trends but of the same order of magnitude in our parameter regime.

5. Conclusion

The above speculation on the -3 scaling mechanism for a scalar spectrum requires diffusivity to be important. This means that the inverse of scalar diffusive time scale needs to be around the onset frequency f_t of the -3 subrange. A direct verification of this hypothesis may be accomplished by investigation of the diffusive and spectral transfer budgets of the scalar fluctuations at the -3 subrange by direct numerical simulations similar to what Pandey *et al.* (2020) did. Our hypothesis will be confirmed if within the -3 subrange, the spectral transfer of the scalar fluctuation (behaving as $T_\theta \propto k^{-1}$) is balanced by the diffusive dissipation ($2\kappa k^2 E_\theta(k)$).

To conclude, when a swarm of high-Reynolds number bubbles are injected into a turbulent thermal mixing layer ($0.3\% \leq \alpha \leq 5.2\%$), the scalar spectra that originally

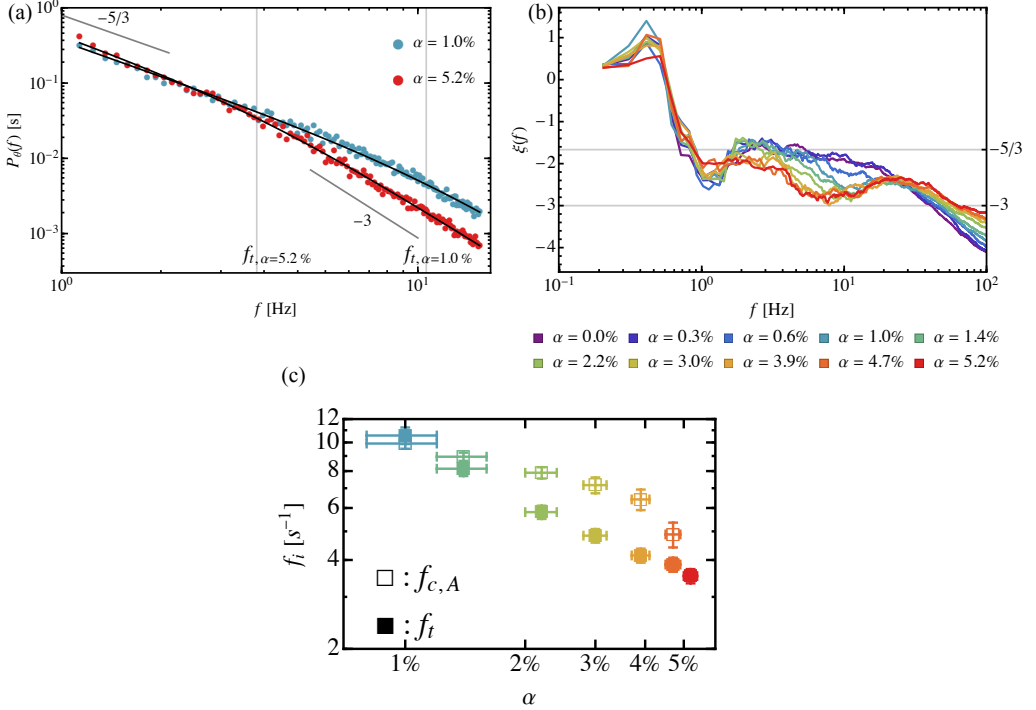


FIGURE 3. (a) The power spectral densities $P_\theta(f)$ of the temperature fluctuation from the measurements (dots) and the corresponding fits (Eq. 4.1) in logarithmic scale for the gas volume fractions $\alpha = 1.0\%$ and $\alpha = 5.2\%$ at the frequency range of 1.2 Hz to 15 Hz (colors same as Fig. 2), plotted together to the purpose of showing the quality of the fits. The two grey sloped lines labeled with ‘ $-5/3$ ’ and ‘ -3 ’ indicate the scaling behaviours of the two limits. The vertical grey lines labeled by f_t indicate the fitted transition frequency for the two cases. (b) The local scaling exponent $\xi(f)$ (defined by Eq. 4.2) of $P_\theta(f)$ over an interval of more than three decades for different gas volume fractions α . Two grey horizontal lines indicates the the slopes $-5/3$ and -3 . The details of obtaining the local slope is described in Section 4. (c) Comparison of $f_{c,A}(\alpha)$ (open symbols, Eq. 4.3) and $f_t(\alpha)$ (solid symbols). The uncertainty of α is related to the precision of the differential pressure gauge (Gvoždić *et al.* (2019)). while the error bars of f_d and $f_{c,A}$ are the confidence intervals from the fitting Eq. 4.1 for a 95% confidence level. The the fitting results of f_t are also tabulated in Table 2.

have a $-5/3$ scaling, for large frequencies develop a steeper -3 slope for larger gas concentration α . As opposed to the energy spectra, which abruptly developed a -3 scaling with the enhancement of the small-scale content for non-zero α , the change of spectral scaling for passive scalar spectra is more gradual by smoothing out the small-scale content when α increases. While the -3 scaling at $\mathcal{O}(100\text{Hz})$ of the energy spectra is attributed to the balance of the production of velocity fluctuations due to bubbles and the molecular viscous dissipation, we speculate that the physical mechanism of the steeper spectral slope in the passive scalar spectra is due to enhanced mixing of bubbles that promotes the homogenization of small-scale temperature differences. The scaling saturates to -3 around $\mathcal{O}(10\text{ Hz})$ when the smoothing of temperature fluctuations is so strong such that the local net transfer of the spectral fluctuation is directly diffused by molecular diffusivity. The transition frequency f_t from the $-5/3$ to -3 scaling in the scalar spectra are obtained from the parameterization (Eq. 4.1) and found to monotonically decrease with increasing α .

In our experiments we had $\text{Pr} = 6.5$ at 22.7°C . This Pr could experimentally be

changed in a certain narrow regime by changing the water temperature (e.g. $Pr = 12.9$ and $Pr = 2.2$). To explore the Pr -dependence, direct numerical simulations would be most welcome. Note however that the much smaller Pr numbers of liquid metal (e.g. $Pr \approx 0.006$ for liquid sodium at 570 K, see Cioni *et al.* (1997)) are again experimentally accessible and that the fluctuations of the temperature in turbulent bubbly sodium may be relevant for applications in working facilities in nuclear power station.

Acknowledgments. We thank Dennis P.M. van Gils, Gert-Wim Bruggert, and Martin Bos for the technical support. We thank Timothy Chan and Jack Cheung for preliminary measurements.

Funding statement. This work was supported by The Netherlands Center for Multiscale Catalytic Energy Conversion (MCEC), an NWO Gravitation Programme funded by the Ministry of Education, Culture and Science of the government of The Netherlands. Chao Sun acknowledges the financial support from Natural Science Foundation of China under Grant nos. 11988102 and 91852202.

Declare of interests. The authors report no conflict of interest.

Appendix A. Method of calculating the energy and scalar spectra in two-phase flow

The hot-film voltage $E_{hf}(t)$ is measured over time. We remove parts of the signal where bubbles interact with the sensor using a threshold method on the time derivative of the measured voltage across the hot-film (see Rensen *et al.* (2005a) and the references therein) or the time derivative of the liquid velocity (Alméras *et al.* (2017)). During a bubble collision with a probe, there is rapid changes of E_{hf} , and the typical shapes of $E_{hf}(t)$ when bubbles colliding with a hot-film can be found in, for example, Rensen *et al.* (2005a) and Rensen *et al.* (2005b). In this work, by inspection of the derivative dE_{hf}/dt over time, a fixed threshold $|dE_{hf}/dt| \geq 500$ V/s is used to detect the moments when bubbles are colliding the probe. We find that the findings and the conclusions of this work are robust against the threshold values within a reasonable range. Apart from the said threshold, we also set the minimal time between two successive bubble collisions (5 ms) in order to determine the moments when bubbles impinging and leaving the probe and to capture the entire bubble interaction events. We check the latter threshold by examining the distributions of the bubble residence time and any unphysical bumps present in the energy spectra due to many unphysically short bubble collisions. To calculate the velocity power spectra, we use the Bartlett Method (Oppenheim & Schafer (2009)) with linear interpolations between the ‘gaps’ of the liquid phase velocity over time for each α . Each partition segment (20 s) cover at least one turnover time by inspecting the auto-correlation function of the signal. Linear interpolation between the gaps of the liquid signal to calculate the power spectra was also used in Alméras *et al.* (2016, 2017). The discussion on the effects of using linear interpolation can be found in Rensen *et al.* (2005a) and Alméras *et al.* (2016).

For the computation of the scalar spectra, we did not create gaps of the temperature time series to distinguish between the gas and liquid phases. This is mainly due to that the response time of the thermistor is comparable to the bubble residence time and the bubbles have similar temperature as the surrounding liquid, which is discussed and shown in Dung (2021). The Bartlett method (Oppenheim & Schafer (2009)) is applied to the temperature signal using partition segments of 10 sec which cover at least one turnover time which was found by inspecting the auto-correlation function of the signal.

REFERENCES

ALMÉRAS, E., CAZIN, S., ROIG, V., RISSO, F., AUGIER, F. & PLAIS, C. 2016 Time-resolved measurement of concentration fluctuations in a confined bubbly flow by LIF. *International Journal of Multiphase Flow* **83** (C), 153–161.

ALMÉRAS, E., MATHAI, V., LOHSE, D. & SUN, C. 2017 Experimental investigation of the turbulence induced by a bubble swarm rising within incident turbulence. *Journal of Fluid Mechanics* **825**, 1091–1112.

BALACHANDAR, S. & EATON, J. K. 2010 Turbulent Dispersed Multiphase Flow. *Annual Review of Fluid Mechanics* **42** (1), 111–133.

BRANDT, L. & COLETTI, F. 2022 Particle-Laden Turbulence: Progress and Perspectives. *Annual Review of Fluid Mechanics* **54** (1), 159–189.

DE BRUYN KOPS, S. M. & RILEY, J. J. 2000 Re-examining the thermal mixing layer with numerical simulations. *Physics of Fluids* **12** (1), 185–192.

CIONI, S., HORANYI, S., KREBS, L. & MÜLLER, U. 1997 Temperature fluctuation properties in sodium convection. *Physical Review E* **56** (4), R3753–R3756.

CORRSIN, S. 1951 On the Spectrum of Isotropic Temperature Fluctuations in an Isotropic Turbulence. *Journal of Applied Physics* **22** (4), 469–473.

DUNG, O.-Y. 2021 Scalars in bubbly turbulence. PhD thesis, University of Twente.

GVOZDIĆ, B., ALMÉRAS, E., MATHAI, V., ZHU, X., VAN GILS, D. P. M., VERZICCO, R., HUISMAN, S. G., SUN, C. & LOHSE, D. 2018 Experimental investigation of heat transport in homogeneous bubbly flow. *Journal of Fluid Mechanics* **845**, 226–244.

GVOZDIĆ, B., DUNG, O.-Y., VAN GILS, D. P. M., BRUGGERT, G.-W. H., ALMÉRAS, E., SUN, C., LOHSE, D. & HUISMAN, S. G. 2019 Twente mass and heat transfer water tunnel: Temperature controlled turbulent multiphase channel flow with heat and mass transfer. *Review of Scientific Instruments* **90** (7), 075117.

JAYESH, TONG, C. & WARHAFT, Z. 1994 On temperature spectra in grid turbulence. *Physics of Fluids* **6** (1), 306–312.

KOLMOGOROV, A. N. 1941 The local structure of turbulence in incompressible viscous fluid for very large reynolds numbers. *Cr Acad. Sci. URSS* **30**, 301–305.

LANCE, M. & BATAILLE, J. 1991 Turbulence in the liquid phase of a uniform bubbly air–water flow. *Journal of Fluid Mechanics* **222**, 95–118.

LOHSE, D. 2018 Bubble puzzles: From fundamentals to applications. *Physical Review Fluids* **3** (11), 110504.

LOHSE, D. & XIA, K.-Q. 2010 Small-scale properties of turbulent Rayleigh–Bénard convection. *Annual Review of Fluid Mechanics* **42**, 335–364.

MA, B.-K. & WARHAFT, Z. 1986 Some aspects of the thermal mixing layer in grid turbulence. *Physics of Fluids* **29** (10), 3114.

MATHAI, V., LOHSE, D. & SUN, C. 2020 Bubbly and Buoyant Particle–Laden Turbulent Flows. *Annual Review of Condensed Matter Physics* **11** (1), 529–559.

MAZZITELLI, I. M. & LOHSE, D. 2009 Evolution of energy in flow driven by rising bubbles. *Physical Review E* **79** (6), 066317.

MONIN, A. S. & YAGLOM, A. M. 1975 *Statistical Fluid Mechanics*. The MIT Press, Cambridge, MA.

MYDLARSKI, L. & WARHAFT, Z. 1998 Passive scalar statistics in high-Péclet-number grid turbulence. *Journal of Fluid Mechanics* **358**, 135–175.

OBUKHOV, A. M. 1949 Temperature field structure in a turbulent flow. *Izv. Acad. Nauk SSSR Ser. Geog. Geofiz* **13**, 58–69.

OPPENHEIM, A. V. & SCHAFER, R. W. 2009 *Discrete-Time Signal Processing, Third Edition*. Prentice Hall Press, Upper Saddle River, NJ.

PANDEY, V., RAMADUGU, R. & PERLEKAR, P. 2020 Liquid velocity fluctuations and energy spectra in three-dimensional buoyancy-driven bubbly flows. *Journal of Fluid Mechanics* **884**, R6.

POPE, S. B. 2000 *Turbulent Flows*. Cambridge University Press, Cambridge, England.

PRAKASH, V. N., MERCADO, J. M., VAN WIJNGAARDEN, L., MANCILLA, E., TAGAWA, Y., LOHSE, D. & SUN, C. 2016 Energy spectra in turbulent bubbly flows. *Journal of Fluid Mechanics* **791**, 174–190.

RENSEN, J., LUTHER, S. & LOHSE, D. 2005a The effect of bubbles on developed turbulence. *Journal of Fluid Mechanics* **538**, 153–187.

RENSEN, J., LUTHER, S., DE VRIES, J. & LOHSE, D. 2005b Hot-film anemometry in bubbly flow I: bubble–probe interaction. *International Journal of Multiphase Flow* **31** (3), 285–301.

RIBOUX, G., LEGENDRE, D. & RISSO, F. 2013 A model of bubble-induced turbulence based on large-scale wake interactions. *Journal of Fluid Mechanics* **719**, 362–387.

RIBOUX, G., RISSO, F. & LEGENDRE, D. 2010 Experimental characterization of the agitation generated by bubbles rising at high Reynolds number. *Journal of Fluid Mechanics* **643**, 509–539.

RISSO, F. 2018 Agitation, Mixing, and Transfers Induced by Bubbles. *Annual Review of Fluid Mechanics* **50** (1), 25–48.

SCHLICHTING, H. & GERSTEN, K. 2017 *Boundary-layer theory*. Springer-Verlag, Berlin, Heidelberg.

STEINBERG, V. 2020 Elastic Turbulence: An Experimental View on Inertialess Random Flow. *Annual Review of Fluid Mechanics* **53** (1), 1–32.

STEINHART, J. S. & HART, S. R. 1968 Calibration curves for thermistors. *Deep Sea Research and Oceanographic Abstracts* **15** (4), 497–503.

VALENTE, P. C. & VASSILICOS, J. C. 2012 Universal Dissipation Scaling for Nonequilibrium Turbulence. *Physical Review Letters* **108** (21), 214503.

VASSILICOS, J. C. 2015 Dissipation in Turbulent Flows. *Annual Review of Fluid Mechanics* **47** (1), 1–20.

YASUDA, T., GOTOH, T., WATANABE, T. & SAITO, I. 2020 Péclet-number dependence of small-scale anisotropy of passive scalar fluctuations under a uniform mean gradient in isotropic turbulence. *Journal of Fluid Mechanics* **898**, A4.